Lattice dynamics of photoexcited insulators from constrained density-functional perturbation theory

Giovanni Marini [1] and Matteo Calandra [1,2]
[1] *Graphene Labs, Fondazione Istituto Italiano di Tecnologia, Via Morego, I-16163 Genova, Italy*
[2] *Department of Physics, University of Trento, Via Sommarive 14, 38123 Povo, Italy*

(Received 22 June 2021; revised 22 September 2021; accepted 24 September 2021; published 7 October 2021)

We present a constrained density-functional perturbation theory scheme for the calculation of structural and harmonic vibrational properties of insulators in the presence of an excited and thermalized electron-hole plasma. The method is ideal to tame ultrafast light-induced structural transitions in the regime where the photocarriers thermalize faster than the lattice, the electron-hole recombination time is longer than the phonon period, and the photocarrier concentration is large enough to be approximated by an electron-hole plasma. The complete derivation presented here includes total energy, forces and stress tensor, variable cell structural optimization, harmonic vibrational properties, and the electron-phonon interaction. We discuss in detail the case of zone-center optical phonons not conserving the number of electrons and inducing a Fermi shift in the photoelectron and hole distributions. We validate our implementation by comparing with finite differences in Te and VSe_2. By calculating the evolution of the phonon spectrum of Te, Si, and GaAs as a function of the fluence of the incoming laser light, we demonstrate that even at low fluences, corresponding to approximately 0.05 photocarriers per atom, the phonon spectrum is substantially modified with respect to the ground-state one with new Kohn anomalies appearing and a substantial softening of zone-center optical phonons. Our implementation can be efficiently used to detect reversible transient phases and irreversible structural transitions induced by ultrafast light absorption.

DOI: 10.1103/PhysRevB.104.144103

I. INTRODUCTION

The development of density-functional perturbation theory (DFPT) approaches [1–6] has allowed for efficient calculations of the ground-state linear response properties of materials without need of supercells. DFPT is nowadays routinely employed to calculate ground-state properties such as force constants and harmonic phonon dispersions [1–3,6], dielectric tensors and Born effective charges [1,4,6], the electron-phonon interaction [5,7,8], Hubbard parameters [9], and nonadiabatic phonon dispersions [10], just to name a few. DFPT assumes electrons to be in the ground state, occupying the lowest-energy Kohn-Sham orbitals, and then exploits analytic expressions of the derivative of the total energy with respect to parameters external to the electronic system such as the ionic displacements or applied electric fields present in the external potential. Its accuracy and capabilities are demonstrated by its widespread use in modern condensed matter theory [4].

The developments of ultrafast spectroscopic techniques and pump-probe experiments have opened new perspectives in condensed matter physics and chemistry (see Ref. [11]). In semiconductors, femtosecond laser pulses can promote a substantial number of electrons from valence to conduction bands; concentrations in excess of 10^{22} cm^{-3} photoexcited carriers can be readily achieved [12], corresponding to approximately 0.2 excited electrons per atom in silicon. As the thermalization of photoexcited carriers typically occurs within hundreds of femtoseconds, the system experiences an electron-hole plasma at times that are typically smaller than the phonon period (a few picoseconds). Until electron-hole recombination takes place (in large-gap insulators, electron-hole recombination is slower than the typical lattice timescale, the precise value depending on the electron-hole plasma density) the lattice effectively feels a thermalized electron-hole distribution.

As the first optically active empty bands of semiconductors are typically composed of antibonding states, their occupation determines a substantial variation of the crystal potential and can lead to an ultrafast destabilization of the crystal structure (on the picosecond scale, i.e., much faster than what can be achieved with thermal processes). The sample can then undergo a structural transition towards a reversible transient phase that is lost after electron-hole recombination (i.e., the system goes back to its ground state), or it can undergo an irreversible structural transition. In the first case, the transient phase can be detected either by ultrafast x-ray diffraction at x-ray free-electron laser facilities [13] or by pump-probe experiments to measure reflectivity, optical absorption, the dielectric function, or Raman spectra after the electronic excitation [14,15]. In the second case, any experimental technique can be used to characterize the sample as the phase is stable even after removal of the laser source. Examples of this second class of transition are phase change materials [13] and nonthermal melting of semiconductors above critical fluence values [16,17]. A plethora of light-induced phenomena have

been observed, including various kinds of electronic phase transitions [18–20], order-disorder transitions [21], structural transformations [22], light-induced charge transfer [23], detection of warm dense matter [24], phonon softenings [25], and nonlinear phononic effects [26,27].

This broad range of phenomena calls for efficient theoretical approaches to compute the structural properties of insulators and semiconductors in the presence of a thermalized electron-hole plasma. In this paper we develop a constrained DFPT framework to calculate the forces acting on the ions, the stress tensor (allowing for cell relaxation), the force constant matrix, the phonon dispersion, and the electron-phonon interaction in the presence of a thermalized electron-hole plasma. Our work is based on previous works by Tangney and Fahy [28,29] and Murray *et al.* [30], where the authors developed total energy and lattice response calculations in the presence of two different chemical potentials, one for the thermalized holes and one for the thermalized electrons. Moreover, as the presence of a substantial photocarrier concentration (PC) leads to a metallic state, we generalize the developments of density-functional perturbation theory for metals carried out in Ref. [3] to the case of two different chemical potentials for electrons and holes, with particular care for the case of zone-center phonons and the treatment of the Fermi shifts induced by the perturbation.

We apply the method to photoexcited tellurium, silicon, gallium arsenide, and vanadium diselenide. We show that, even at the lowest considered PC, the phonon spectrum is substantially affected and cannot be considered to be the same as the ground state. We systematically compare our method with the widespread technique of simulating light excitation with a single Fermi-Dirac distribution with an electronic temperature of the same order as the incoming photon energy (see, e.g., Refs. [31,32]). We demonstrate that the latter approximation cannot be applied to photoexcited semiconductors and insulators as it leads to inconsistent results when comparing with experiments, notably when cell relaxation is taken into account. In contrast, our implementation based on two Fermi distributions, one for the thermalized holes and one for the thermalized electrons, leads to better agreement with experiments at an affordable computational cost.

The paper is structured as follows. In Sec. II we illustrate the fundamental assumptions behind the present framework, and in Secs. III, IV, and V we illustrate the mathematical formalism. Section VI contains a description of our methods, while in Sec. VII we present some relevant applications, followed by conclusions in Sec. VIII.

II. INHERENT ASSUMPTIONS IN THE THERMALIZED ELECTRON-HOLE PLASMA MODEL

The thermalized electron-hole plasma model (also labeled the two-distribution model in the following) assumes that, for times that are of the order of the phonon period, the photoexcited insulator or semiconductor can be described by a thermalized electron-hole plasma identified by two different chemical potentials (see Fig. 1). We are thus assuming the following:

(i) Photoexcited electrons and holes thermalize within hundreds of femtoseconds.

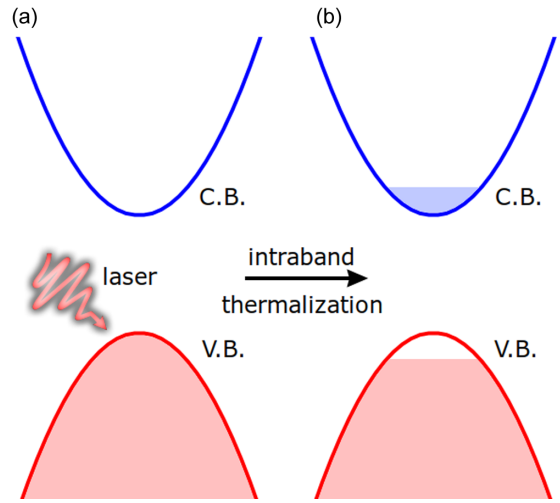

FIG. 1. Schematic representation of the effect of laser irradiation on electronic occupations. (a) Electronic distribution before laser irradiation. (b) Electronic distribution after laser irradiation, after intraband thermalization but before electron-hole recombination takes place. C.B., conduction band; V.B., valence band.

(ii) Electron-hole recombination times are much longer than the phonon period.

These two assumptions are usually satisfied in experiments on insulators and large-gap semiconductors as the phonon period is of the order of a few picoseconds, while the electron-hole recombination is generally much slower [33,34]. While the carrier recombination time is known to decrease with increasing density, theoretical arguments and experimental observations indicate that this behavior saturates at high density for the main recombination mechanisms (radiative and Auger recombination) [35–37], thus justifying our treatment. This conclusion is also supported by the experiments of Hunsche *et al.* [38] on semiconducting tellurium, which demonstrate no significant change in the A_1 phonon lifetime as a function of the carrier density, contrary to what one would have observed had the electron-hole recombination occurred on a timescale comparable to the phonon period [3]. In metals, in general, carrier recombination is very fast, and the model is inappropriate. However, in some cases, the metal can be seen as a hole-doped insulator and a part of the excitations occurs across an energy gap; thus carrier recombination could still be slow enough for the application of the two-distribution model. Finally, in the case of semimetals such as Bi and Sb, it has been shown that a two-chemical-potential approach correctly explains the displacive excitations of coherent phonons [39]. The physical reason is probably related to the fact that in a semimetal, the vanishing density of states at the Fermi level acts as a bottleneck for the electron-hole recombination. However, the validity of the method for metals and semimetals has to be checked carefully case by case.

We also assume that the excited electron and hole population is large enough to be approximated by an electron-hole plasma. Indeed, while the low-PC regime is characterized by the occurrence of a resonant peak in correspondence to the exciton energy (see, for example, Refs. [40–43]), when the PC reaches a critical value, the system undergoes a transition

TABLE I. Predicted band gaps for bulk tellurium, silicon, and GaAs compared with the experimental value at room temperature.

	Gap	
Material	Theor.	Expt.
Te	0.18	0.35 [45]
Si	0.45	1.17 [46]
GaAs	1.02	1.52 [46]

towards an electron-hole plasma state [42,43] where excitons are not bound anymore and are completely screened. The critical density for the electron-hole plasma formation depends on the specific system; however, a rough estimation can be given in terms of the material-dependent exciton Bohr radius [44], i.e., the radius associated with the exciton. The electron-hole pairs condense in the plasma state once the average distance between them becomes smaller than this quantity. In the electron-hole plasma regime, the laser pumps electrons to single-particle conduction-band states. This requires that the single-particle states (i.e., the Kohn-Sham energies) correctly describe the single-particle excitations across the gap. It is known that density-functional theory (DFT) with semilocal functionals typically underestimates band gaps (see Table I), and consequently the inclusion of a self-energy correction such as Hedin's *GW* approximation (GW) may be necessary to obtain a correct description of photoexcitation. However, if the self-energy correction on the conduction eigenstates is well approximated by a scissor operator, calculations can be performed within semilocal DFT, and the gap correction can be accounted for *a posteriori* with a rigid shift ΔE_{GW} whenever a comparison to the experimental laser energy is required. Finally, we underline that in all applications considered in this paper we verified that the bottom of the conduction band is a bright state. In principle that is not required as the present formalism can also be applied to the case of a dark first excited state (i.e., not allowed by dipole selection rules) by properly initializing the simulation in such a way as to fulfill the optical transition matrix element (see Ref. [28] for more details).

We now proceed to obtain the expressions for the total energy, forces, force constant matrices, and electron-phonon coupling in constrained DFPT (cDFPT).

III. TOTAL ENERGY

The derivation presented here closely follows and extends the one given by de Gironcoli [3] for the case of metals. We consider the situation where a fraction of the valence electrons has been excited from the valence to the conduction band. Our hypothesis is that thermal equilibrium is reached separately in both the valence- and the conduction-band subsets, so that it is reasonable to describe electronic occupations in the two subsets with two separate Fermi-Dirac distributions. The smearing function can be a generic smooth approximation to the Dirac δ function; in general, different temperatures for valence and conduction distributions are allowed. Similarly to the case of metals, the basic quantity for a practical density-functional theory formulation is the local density of states $n(\mathbf{r},\epsilon)$, which is convoluted with the smearing function $f(\epsilon)=(1/\sigma)\tilde{\delta}(\epsilon/\sigma)$. In the present case, valence- and conduction-band distributions are separately convoluted with a smearing function. We assume that the first N_v bands are the valence bands. The resulting expression for the local density of states is

$$n(\mathbf{r},\epsilon)=\sum_{i=1}^{N_v}\frac{1}{\sigma}\tilde{\delta}\Big(\frac{\epsilon-\epsilon_i}{\sigma}\Big)|\phi_i(\mathbf{r})|^2 + \sum_{i=N_v+1}^{\infty}\frac{1}{\sigma_c}\tilde{\delta}\Big(\frac{\epsilon-\epsilon_i}{\sigma_c}\Big)|\phi_i(\mathbf{r})|^2, \tag{1}$$

where ϵ_i and $\phi_i(\mathbf{r})$ are the Kohn-Sham eigenvalues and eigenfunctions, respectively, σ and σ_c represent the smearing parameters for the valence and conduction carriers, respectively, and the summation over $\mathbf{k}$ points and spin is implicit. We work under the hypothesis that the valence and conduction bands are separated by an energy gap E_g much larger than the smearing values, $E_g \gg \max(\sigma,\sigma_c)$. In the case of Fermi-Dirac occupations, σ and σ_c represent the two temperatures of the valence and conduction carriers. The electron density is

$$n(\mathbf{r})=\int_{-\infty}^{\epsilon_F} n(\mathbf{r},\epsilon)d\epsilon+\int_{E_c}^{\epsilon'_F} n(\mathbf{r},\epsilon)d\epsilon \;=\sum_i \Theta_i^{F,F'}|\phi_i(\mathbf{r})|^2, \tag{2}$$

where E_c is the minimum of the conduction band, ϵ_F and ϵ'_F denote the valence and conduction quasi-Fermi-levels, and the function $\tilde{\Theta}_i^{F,F'}$ is case defined as the integral of the $\tilde{\delta}$ in one of the two band sets:

$$\tilde{\Theta}_i^{F,F'}=\begin{cases}\tilde{\theta}\big(\frac{\epsilon_i-\epsilon_F}{\sigma}\big), & i=1,N_v\\ \tilde{\theta}'\big(\frac{\epsilon_i-\epsilon'_F}{\sigma_c}\big), & i=N_v+1,\infty,\end{cases} \tag{3}$$

where $\tilde{\theta}(x)=\int_{-\infty}^{x}\tilde{\delta}(y)dy$ and $\tilde{\theta}'(x)=\int_{E_c}^{x}\tilde{\delta}(y)dy$. The quasi-Fermi-levels are determined imposing conservation of the number of particles in valence and conduction bands, $N_{el}^{v,c}$, separately:

$$N_{el}=N_{el}^v+N_{el}^c,\quad N_{el}^v=\int_{-\infty}^{\epsilon_F}n(\epsilon)d\epsilon=\sum_{i=1}^{N_v}\tilde{\theta}\Big(\frac{\epsilon_F-\epsilon_i}{\sigma}\Big),$$
$$N_{el}^c=\int_{E_c}^{\epsilon'_F}n(\epsilon)d\epsilon=\sum_{i=N_v+1}^{\infty}\tilde{\theta}'\Big(\frac{\epsilon'_F-\epsilon_i}{\sigma_c}\Big), \tag{4}$$

where $n(\epsilon)$ is the density of states. In analogy with the case of a metal, the kinetic Kohn-Sham functional $T_s[n]$ is defined through the Legendre transform of the single-particle energy integral and is written

$$T_s[n]=\int_{-\infty}^{\epsilon_F}\epsilon n(\epsilon)d\epsilon+\int_{E_c}^{\epsilon'_F}\epsilon n(\epsilon)d\epsilon-\int V_{\mathrm{SCF}}(\mathbf{r})n(\mathbf{r})d\mathbf{r}$$
$$=\sum_i\left[-\frac{\hbar^2}{2m}\Theta_i^{F,F'}\langle\phi_i|\nabla^2|\phi_i\rangle+\tilde{\Theta}_i^{1,F,F'}\right], \tag{5}$$

where the self-consistent potential $V_{\mathrm{SCF}}(\mathbf{r})$ is defined in terms of the external potential $V(\mathbf{r})$ and the exchange and correlation

functional E_{xc} as [4]

$$V_{\rm SCF}(\mathbf{r}) = V(\mathbf{r}) + e^2 \int \frac{n(\mathbf{r}')}{|\mathbf{r}-\mathbf{r}'|} d\mathbf{r}' + v_{xc}(\mathbf{r})$$
$$v_{xc} = \frac{\delta E_{xc}}{\delta n(\mathbf{r})}, \tag{6}$$

and we introduced the function $\tilde{\Theta}_i^{1,F,F'}$, which is case defined as

$$\tilde{\Theta}_i^{1,F,F'} = \begin{cases} \sigma\tilde{\theta}_1\left(\frac{\epsilon_i-\epsilon_F}{\sigma}\right), & i = 1, N_v \\ \sigma_c\tilde{\theta}_1{}'\left(\frac{\epsilon_i-\epsilon_F'}{\sigma_c}\right), & i = N_v+1, \infty, \end{cases} \tag{7}$$

where $\tilde{\theta}_1(x) = \int_{-\infty}^{x} y\tilde{\delta}(y)dy$ and $\tilde{\theta}_1'(x) = \int_{E_c}^{x} y\tilde{\delta}(y)dy$.

The total energy can be written in terms of the kinetic functional

$$E[n] = T_s[n] + \frac{e^2}{2}\int \frac{n(\mathbf{r})n(\mathbf{r}')}{|\mathbf{r}-\mathbf{r}'|} d\mathbf{r}d\mathbf{r}' + E_{xc}[n], \tag{8}$$

and with this choice for the kinetic functional the Kohn-Sham equations follow from the minimization of the total energy with respect to the density, imposing the conservation for the number of valence and conduction electrons. As in the case of the metallic system, the drawback of the smearing approach is that total energy depends on the smearing parameter. In the case of two Fermi levels the error in the total energy is the sum of the errors due to valence and conduction smearing convolution; all the other considerations made for the metallic case [3] can be extended to this case.

IV. FORCES AND STRESS TENSOR

With the definition above, forces are computed from the Hellmann-Feynman theorem:

$$\frac{\partial E}{\partial \mathbf{u}_s} = \int n(\mathbf{r}) \frac{\partial V(\mathbf{r})}{\partial \mathbf{u}_s} d\mathbf{r} + \frac{\partial E_{\rm ion}}{\partial \mathbf{u}_s}, \tag{9}$$

where $\mathbf{u}_s$ represents the position of atom s and $E_{\rm ion}$ is the electrostatic energy due to the interaction between the ions. The stress tensor $\alpha_{i,j}$ is defined as minus the derivative of the total energy with respect to the strain $\eta_{i,j}$ divided by the volume:

$$\alpha_{i,j} = -\frac{1}{\Omega}\frac{\partial E_{\rm tot}}{\partial \eta_{i,j}}, \tag{10}$$

where the strain is defined as the space scaling operation $\mathbf{r}_i \to (\delta_{i,j} + \eta_{i,j})\mathbf{r}_j$. With the given definition for the kinetic functional, strain calculation is analogous to the metallic case (see Refs. [47,48] for the complete expression of the stress tensor); pressure is defined as minus the trace of the strain tensor, $P = -\sum_i \alpha_{i,i}$.

V. VIBRATIONAL PROPERTIES

We now come to the description of lattice dynamics in the two-temperature model. The force constant matrix is obtained as the derivative of the Hellmann-Feynman force:

$$\mathbf{\Phi}_{s,s'} = \int \frac{\partial n(\mathbf{r})}{\partial \mathbf{u}_s}\frac{\partial V(\mathbf{r})}{\partial \mathbf{u}_{s'}} d\mathbf{r} + \int n(\mathbf{r}) \frac{\partial^2 V(\mathbf{r})}{\partial \mathbf{u}_s \partial \mathbf{u}_{s'}} d\mathbf{r} \quad + \frac{\partial^2 E_{\rm ion}}{\partial \mathbf{u}_s \partial \mathbf{u}_{s'}}. \tag{11}$$

We then proceed with the calculation of the density variation following an infinitesimal lattice perturbation. We start by considering the generic density response to a perturbation, by direct variation of Eq. (2):

$$\Delta n(\mathbf{r}) = \sum_i \Theta_i^{F,F'}[\phi_i^*(\mathbf{r})\Delta\phi_i(\mathbf{r}) + \text{c.c.}] + \sum_i |\phi_i(\mathbf{r})|^2 \tilde{\Delta}_i^{F,F'}(\Delta\epsilon^{F,F'} - \Delta\epsilon_i), \tag{12}$$

where

$$\tilde{\Delta}_i^{F,F'} = \begin{cases} (1/\sigma)\tilde{\delta}\left(\frac{\epsilon_i-\epsilon_F}{\sigma}\right), & i = 1, N_v \\ (1/\sigma_c)\tilde{\delta}\left(\frac{\epsilon_i-\epsilon_F'}{\sigma_c}\right), & i = N_v+1, \infty \end{cases} \tag{13}$$

and

$$\Delta\epsilon^{F,F'} = \begin{cases} \Delta\epsilon_F, & i = 1, N_v \\ \Delta\epsilon_F', & i = N_v+1, \infty. \end{cases} \tag{14}$$

The term due to the Fermi shift, $\Delta\epsilon^{F,F'}$, will be addressed in Sec. V A. The first-order correction to the eigenfunction is orthogonal to the eigenfunction itself and can be expressed in terms of a sum over the spectrum of the perturbed Hamiltonian:

$$\Delta\phi_i(\mathbf{r}) = \sum_{j\neq i} \phi_i(\mathbf{r}) \frac{\langle\phi_j|\Delta V_{\rm SCF}|\phi_i\rangle}{\epsilon_i - \epsilon_j}, \tag{15}$$

where $\Delta V_{\rm SCF}$ is the variation of the self-consistent potential [Eq. (6)]

$$\Delta V_{\rm SCF}(\mathbf{r}) = \Delta V(\mathbf{r}) + e^2 \int \frac{\Delta n(\mathbf{r}')}{|\mathbf{r}-\mathbf{r}'|} d\mathbf{r}' + \frac{dv_{xc}(n)}{dn}\Delta n(\mathbf{r}). \tag{16}$$

We substitute the expression for the wave-function variation given in Eq. (15) into Eq. (12) and specialize to the case of an infinitesimal lattice perturbation:

$$\frac{\partial n(\mathbf{r})}{\partial \mathbf{u}_s} = \sum_{i,j} \frac{\tilde{\Theta}_i^{F,F'} - \tilde{\Theta}_j^{F,F'}}{\epsilon_i - \epsilon_j} \phi_i(\mathbf{r})^*\phi_j(\mathbf{r}) \left\langle \phi_j \middle| \frac{\partial V_{\rm SCF}}{\partial \mathbf{u}_s} \middle| \phi_i \right\rangle. \tag{17}$$

Using the relation $\tilde{\theta}(x) + \tilde{\theta}(-x) = 1$ and the symmetry in exchanging i and j, we rewrite

$$\frac{\partial n(\mathbf{r})}{\partial \mathbf{u}_s} = 2\sum_{i,j} \frac{\tilde{\Theta}_i^{F,F'} - \tilde{\Theta}_j^{F,F'}}{\epsilon_i - \epsilon_j} \theta_{j,i} \times \phi_i(\mathbf{r})^*\phi_j(\mathbf{r}) \left\langle \phi_j \middle| \frac{\partial V_{\rm SCF}}{\partial \mathbf{u}_s} \middle| \phi_i \right\rangle. \tag{18}$$

Here, $\tilde{\theta}_{i,j} = \tilde{\theta}[(\epsilon_i - \epsilon_j)/\sigma]$, the first index runs only over the partially occupied states, and the second one runs only over those partially unoccupied. We further simplify the expression by avoiding the sum over the unoccupied states,

writing

$$\frac{\partial n(\mathbf{r})}{\partial \mathbf{u}_s} = 2\sum_i \phi_i(\mathbf{r})^* \Delta\phi_i(\mathbf{r}), \tag{19}$$

where $\Delta\phi_i$ satisfies

$$\begin{aligned}
[H_{\mathrm{SCF}} + Q - \epsilon_i]\Delta\phi_i &= -\left[\tilde{\Theta}_i^{F,F'} - P_i\right]\frac{\partial V_{\mathrm{SCF}}}{\partial \mathbf{u}_s}|\phi_i\rangle\,, \\
Q &= \sum_k \alpha_k |\phi_k\rangle\langle\phi_k|\,, \\
P_i &= \sum_j \beta_{i,j}|\phi_j\rangle\langle\phi_j|\,, \\
\beta_{i,j} &= \tilde{\Theta}_i^{F,F'}\tilde{\theta}_{i,j} + \tilde{\Theta}_j^{F,F'}\tilde{\theta}_{j,i} \\
&\quad + \alpha_j\frac{\tilde{\Theta}_{F,i} - \tilde{\Theta}_{F,j}}{\epsilon_i - \epsilon_j}\tilde{\theta}_{j,i},
\end{aligned} \tag{20}$$

where H_{SCF} is the unperturbed Kohn-Sham Hamiltonian [4]. Here, α_k's are chosen in such a way that the Q operator makes the linear system given in Eq. (20) nonsingular for all nonvanishing $\Delta\phi_k$. A possible simple choice is $\alpha_k = \max(\epsilon'_F + \Delta - \epsilon_k, 0)$. Another choice is to set α_k equal to the occupied bandwidth plus a certain quantity, e.g., 3σ, for all (partially) occupied states and equal to zero for totally unoccupied states.

A. Zone-center phonons inducing Fermi shifts

In this section we discuss the peculiarities related to the calculation of the linear response for optical zone-center phonons. In DFPT (and cDFPT) codes the phonon calculations with $\mathbf{q} \neq \mathbf{0}$ and $\mathbf{q} = \mathbf{0}$ are treated with two different approaches. At $\mathbf{q} \neq \mathbf{0}$, the calculation is performed within the grand canonical ensemble, with a constant electron chemical potential (in our case, with two constant chemical potentials—electron and hole). At $\mathbf{q} = \mathbf{0}$, the calculation is performed in the canonical ensemble with a constant number of electrons. When the phonon displacement induces a change in the number of the electrons, a Fermi shift has to be included to enforce charge conservation. In our framework this amounts to introducing two Fermi shifts for the two quasi-Fermi-levels in the density response:

$$\begin{aligned}
\frac{\partial n(\mathbf{r})}{\partial \mathbf{u}_s} &= 2\sum_i \phi_i(\mathbf{r})^*\Delta\phi_i(\mathbf{r}) \\
&\quad + \sum_i |\phi_i(\mathbf{r})|^2 \tilde{\Delta}_i^{F,F'}(\Delta\epsilon^{F,F'} - \Delta\epsilon_i).
\end{aligned} \tag{21}$$

This term can only arise for a periodic perturbation at $\mathbf{q} = 0$, in compounds where the atomic positions are not all fixed by symmetry.

The Fourier transform of the self-consistent potential variation, $\Delta V_{\mathrm{SCF}}(\mathbf{q})$, reads

$$\Delta V_{\mathrm{SCF}}(\mathbf{q}) = \frac{4\pi e^2}{q^2}\Delta n_{\mathrm{ext}}(\mathbf{q}) + \frac{4\pi e^2}{q^2}\Delta n(\mathbf{q}) + \frac{dv_{xc}}{dn}\Delta n(\mathbf{q}), \tag{22}$$

which we separate into the contributions due to the valence and conduction electrons $\Delta V_{\mathrm{SCF}}^{v,c}(\mathbf{q})$:

$$\begin{aligned}
\Delta V_{\mathrm{SCF}}(\mathbf{q}) &= \Delta V_{\mathrm{SCF}}^{v}(\mathbf{q}) + \Delta V_{\mathrm{SCF}}^{c}(\mathbf{q}), \\
\Delta V_{\mathrm{SCF}}^{v}(\mathbf{q}) &= \frac{4\pi e^2}{q^2}\Delta n_{\mathrm{ext}}^{v}(\mathbf{q}) + \frac{4\pi e^2}{q^2}\Delta n^{v}(\mathbf{q}) + \frac{dv_{xc}}{dn}\Delta n^{v}(\mathbf{q}), \\
\Delta V_{\mathrm{SCF}}^{c}(\mathbf{q}) &= \frac{4\pi e^2}{q^2}\Delta n_{\mathrm{ext}}^{c}(\mathbf{q}) + \frac{4\pi e^2}{q^2}\Delta n^{c}(\mathbf{q}) + \frac{dv_{xc}}{dn}\Delta n^{c}(\mathbf{q}),
\end{aligned} \tag{23}$$

where $\Delta n_{\mathrm{ext}}^{v,c}(\mathbf{q})$ represent the valence and conduction density variation due to the macroscopic electrostatic component of the perturbing potential. Similarly, we decompose the density variation induced by a generic perturbation, $\Delta n(\mathbf{q})$, into the valence and conduction terms $\Delta n^{v,c}(\mathbf{q})$:

$$\begin{aligned}
\Delta n(\mathbf{q}) &= \Delta n^{v}(\mathbf{q}) + \Delta n^{c}(\mathbf{q}), \\
\Delta n^{v}(\mathbf{q}) &= -n(\epsilon_F)\Delta V_{\mathrm{SCF}}^{v}(\mathbf{q}) + \Delta n_v^{lf}(\mathbf{q}), \\
\Delta n^{c}(\mathbf{q}) &= -n(\epsilon'_F)\Delta V_{\mathrm{SCF}}^{c}(\mathbf{q}) + \Delta n_c^{lf}(\mathbf{q}),
\end{aligned} \tag{24}$$

where $\Delta n_{v,c}^{lf}$ are the valence and conduction parts of the density response to the nonmacroscopic component of the self-consistent potential. The self-consistent potential variation due to the valence and conduction electrons can then be expressed as

$$\begin{aligned}
\Delta V_{\mathrm{SCF}}^{v}(\mathbf{q}) &= -\frac{\Delta n_v(\mathbf{q}) - \Delta n_v^{lf}(\mathbf{q})}{n(\epsilon_F)}, \\
\Delta V_{\mathrm{SCF}}^{c}(\mathbf{q}) &= -\frac{\Delta n_c(\mathbf{q}) - \Delta n_c^{lf}(\mathbf{q})}{n(\epsilon'_F)}.
\end{aligned} \tag{25}$$

For $\mathbf{q} \approx 0$, we have $\Delta n_{\mathrm{ext}}^{v,c}(\mathbf{q}) = \Delta n^{v,c}(\mathbf{q}) + O(q^2)$. We enforce charge neutrality applying quasi-Fermi-level shifts equal and opposite to the variation of the macroscopic component of the self-consistent potential felt by valence and conduction electrons:

$$\begin{aligned}
\Delta\epsilon_F &= \frac{\Delta n_{\mathrm{ext}}^{v}(\mathbf{q}=0) - \Delta n_v^{lf}(\mathbf{q}=\mathbf{0})}{n(\epsilon_F)}, \\
\Delta\epsilon'_F &= \frac{\Delta n_{\mathrm{ext}}^{c}(\mathbf{q}=0) - \Delta n_c^{lf}(\mathbf{q}=\mathbf{0})}{n(\epsilon'_F)}.
\end{aligned} \tag{26}$$

For a neutral external perturbation such as an infinitesimal lattice perturbation, atoms are displaced, but the total charge does not change, i.e., $\Delta n_{\mathrm{ext}}^{v,c} = 0$. We thus obtain the final expression for the quasi-Fermi-level shifts

$$\begin{aligned}
\Delta\epsilon_F &= -\frac{\Delta n_v^{lf}(\mathbf{q}=\mathbf{0})}{n(\epsilon_F)} = \frac{\int n(\epsilon_F,\mathbf{r})\frac{\partial V_{\mathrm{SCF}}(\mathbf{r})}{\partial \mathbf{u}_s}d\mathbf{r}}{n(\epsilon_F)}, \\
\Delta\epsilon'_F &= -\frac{\Delta n_c^{lf}(\mathbf{q}=\mathbf{0})}{n(\epsilon'_F)} = \frac{\int n(\epsilon'_F,\mathbf{r})\frac{\partial V_{\mathrm{SCF}}(\mathbf{r})}{\partial \mathbf{u}_s}d\mathbf{r}}{n(\epsilon'_F)}.
\end{aligned} \tag{27}$$

We rewrite Eq. (12) as

$$\Delta'\phi_i(\mathbf{r}) = \Delta\phi_i(\mathbf{r}) + \Delta^{sh}\phi_i(\mathbf{r}), \tag{28}$$

where we defined the wave-function shift as

$$\Delta^{sh}\phi_i(\mathbf{r}) = (1/2)\Delta\epsilon^{F,F'}\phi_i(\mathbf{r}). \tag{29}$$

The compact expression for the electron density perturbation is then

$$\frac{\partial n(\mathbf{r})}{\partial \mathbf{u}_s} = 2\sum_i \phi_i(\mathbf{r})^* \Delta' \phi_i(\mathbf{r}). \tag{30}$$

B. Electron-phonon interaction

The last part of our derivation is concerned with the extension of the electron-phonon matrix elements calculation to the case of the two-distribution model. The deformation potential corresponding to a lattice perturbation of momentum $\mathbf{q}$ and irreducible representation ν is written

$$d^{m,n}_{\mathbf{k},\mathbf{q},\nu} = \langle \phi_{\mathbf{k},m} | \frac{\partial V_{\mathrm{SCF}}}{\partial \mathbf{u}_{\mathbf{q},\nu}} | \phi_{\mathbf{k}+\mathbf{q},n} \rangle , \tag{31}$$

where $\mathbf{u}_{\mathbf{q},\nu}$ represents the displacement pattern of momentum $\mathbf{q}$ and irreducible representation ν and $|\phi_{\mathbf{k},m}\rangle$ represents a Kohn-Sham eigenvector characterized by momentum $\mathbf{k}$ and band index m. In the case of two separate carrier distributions, the procedure remains essentially the same, with exceptions made for the case $\mathbf{q} = \mathbf{0}$ and the presence of a nonvanishing Fermi shift for either valence or conduction bands (or both). In this case, the $\mathbf{q} = \mathbf{0}$ component of the calculated potential variation has to be shifted according to Eq. (25) in order to maintain charge neutrality separately in valence and conduction bands. Once this quantity is calculated, the electron-phonon matrix elements $g^{m,n}_{\mathbf{k},\mathbf{q},\nu}$ follow as in standard DFPT [4]:

$$g^{m,n}_{\mathbf{k},\mathbf{q},\nu} = \left(\frac{\hbar}{2\omega_{\mathbf{q},\nu}}\right)^{1/2} d^{m,n}_{\mathbf{k},\mathbf{q},\nu}. \tag{32}$$

VI. METHODS

First-principles calculations have been performed within density-functional theory. We have used scalar-relativistic optimized norm-conserving Vanderbilt pseudopotentials [49] to describe the electron-ion interaction in the case of tellurium and vanadium diselenide and Hartwigsen-Goedecker-Hutter pseudopotentials [50] in the case of gallium arsenide and silicon, while employing a kinetic energy cutoff of 60 Ry (80 Ry for VSe_2) in the plane-wave expansion of the Kohn-Sham wave functions to converge the stress tensor in the variable-cell calculations, as implemented in the QUANTUM ESPRESSO (QE) package [51,52]. The presence of the two quasi-Fermi-surfaces (which we label quasi-FSs) was dealt with using the smearing approach. Two Fermi-Dirac distributions with smearing parameters $\sigma = \sigma_c = 0.05$ eV were considered for Te as in Ref. [28], while the Marzari-Vanderbilt approach [53] was employed for Si, GaAs, and VSe_2, with valence and conduction smearing parameters $\sigma = \sigma_c = 0.136$ eV in order to ensure a converged sampling of the quasi-FSs. For the exchange-correlation potential we have adopted the generalized gradient approximation (GGA) in the Perdew, Burke, and Ernzerhof (PBE) [54] formulation in tellurium and vanadium diselenide, while the local density approximation (LDA) [55] was adopted in silicon and gallium arsenide. In order to ensure a proper relaxation procedure, forces have been relaxed under 1×10^{-5} Ry/bohr. A $16 \times 16 \times 16$ Monkhorst-Pack wave-vector grid [56] has been adopted for the integration of the Brillouin zone (BZ) in silicon and GaAs, a $13 \times 13 \times 10$ grid was employed for tellurium, and a $16 \times 16 \times 9$ grid was used for VSe_2. Phonon frequencies and electron-phonon coupling matrix elements were determined within cDFPT. Phonon frequencies were calculated on a dense $12 \times 12 \times 12$ wave-vector grid for photoexcited Si and GaAs, due to the delicate convergence of the phonon modes as a function of the employed wave-vector grid, attributed to the presence of the two quasi-FSs. Notably, expensive simulations employing a 3456-atom supercell would have been necessary in order to perform the same calculation within the finite-difference approach. The cDFPT formalism described here has been implemented as a modification of the official QE 6.6 release [57].

TABLE II. Structural parameters as a function of PC for tellurium, silicon, and gallium arsenide in the cDFPT approach.

n_e (e/atom)	0	0.015	0.03	0.045	0.06
a (Te) (Å)	4.502	4.506	4.52	4.533	4.546
c/a (Te)	1.325	1.31	1.29	1.27	1.25
x (Te, crystal)	0.271	0.275	0.281	0.287	0.293
n_e (e/atom)	0	0.05	0.1	0.15	0.2
a (Si) (Å)	5.381	5.372	5.365	5.361	5.359
a (GaAs) (Å)	5.527	5.541	5.561	5.583	5.623

VII. APPLICATIONS

A. Tellurium

We apply the presented formalism to the case of bulk tellurium. At ambient conditions the stable phase is α-Te, consisting of helical chains parallel to the c axis of the trigonal $P3_121$-D_3^4 structure [28]. Bulk tellurium has been previously studied in the framework of a two-carrier-distribution model in Ref. [28]. This study attributed the experimentally observed reflectivity oscillations under photoexcitation to the so-called displacive excitation of coherent phonons (DECP) mechanism, caused by the A_1 phonon mode. The motion along the A_1 phonon eigenvector corresponds to a modulation of the free internal coordinate x, representing the helical chain radius. Since the A_1 mode involves the motion of a free internal coordinate, a Fermi shift must occur [10]. As such, α-Te gives us the chance to verify the consistency of our implementation, comparing phonon eigenvalues obtained in finite-difference calculations with those obtained in cDFPT.

We proceed in the following way. First, we calculate the ground-state structure by performing a variable-cell relaxation (see Table II for the structural parameters). We then explore two possible cases: In a first scenario we keep the volume of the unit cell fixed under photoexcitation, as was previously done in Ref. [28]; in a second scenario, we also include the volume change induced by pumping. The reason is the following: The lattice relaxation due to electron photoexcitation can be thought of as an instantaneous change of the Born-Oppenheimer potential felt by the nuclei; consequently, the lattice readjustment is a purely electronic effect. As such, we expect the crystal to readjust to the new lattice parameters in a short timescale, much shorter than the thermal

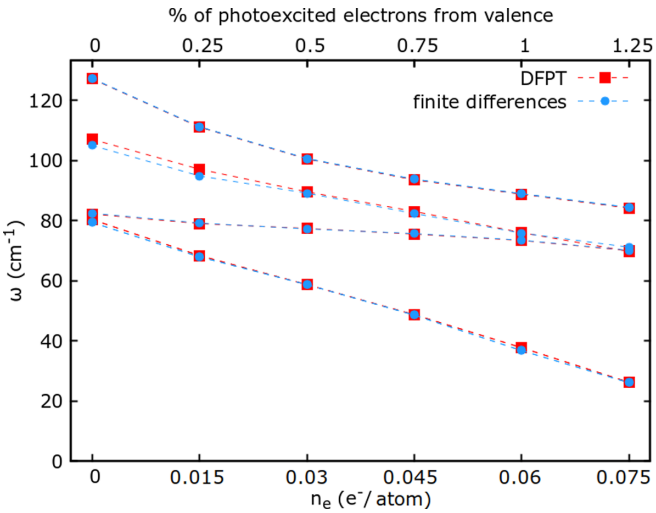

FIG. 2. Phonon frequencies for bulk tellurium at the Γ point as a function of PC, without the effect of volume relaxation. Red lines indicate the results obtained within cDFPT, while blue lines are calculated with the finite-difference method.

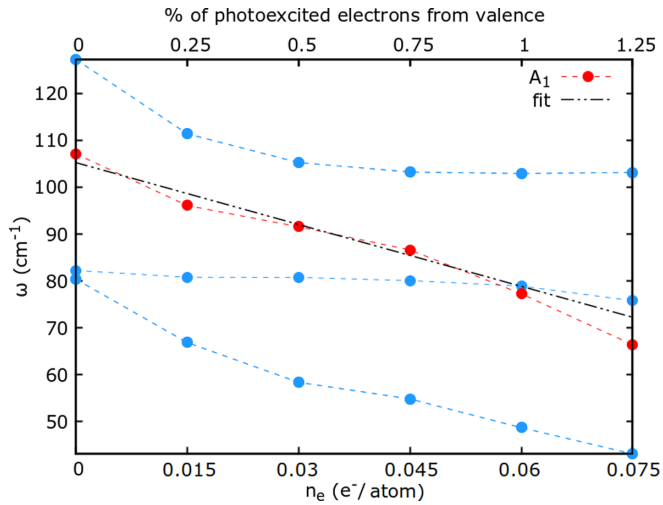

FIG. 3. Phonon frequencies for bulk tellurium at the Γ point as a function of PC, including the effect of volume relaxation. The red line indicates the A_1-symmetry phonon responsible for DECP, and the black line represents the corresponding linear fit.

one, as demonstrated by multiple experimental observations [16,17,58]. While the precise timescale for nonthermal lattice readjustment depends on the size and composition of the sample, from the experimental observations we infer that the typical timescale for a 100-nm-sized silicon sample is less than 1 ps [58]; thus it is physically meaningful to perform variable-cell relaxation at the considered PC value and perform the phonon calculation on the volume-relaxed cell.

First of all, we use the case of tellurium as a benchmark for our implementation, comparing the phonon frequencies obtained within cDFPT with the ones obtained with a finite-difference calculation [59]. The comparison is reported in Fig. 2 demonstrating an excellent agreement between the results in the two approaches, confirming the consistency of our implementation.

Without including volume effects, we obtain a phonon frequency shift of -0.91 THz at $n_e = 0.06$ e/atom, where n_e represents the photocarrier concentration, corresponding to 1% excitation of the valence population. Using the model in Ref. [28] and assuming linearity between the reflectivity changes and phonon frequency shift, we infer that the derivative of the reflectivity peak frequency with respect to pump fluence is equal to -0.08 THz per mJ/cm^2, against the experimental value of -0.07 THz per mJ/cm^2 reported in Ref. [28], obtained by fitting the low-excitation part of the experimental data presented in Ref. [38]. Thus, neglecting cell relaxation, the value is underestimated by ≈14%.

We then proceed to include the effect of the volume change in the frequency calculation. We relax the tellurium structural parameters at each PC. The structural parameters as a function of PC are reported in Table II, while the behavior of phonon frequencies at Γ is shown in Fig. 3. We fit the A_1 mode in the low-photoexcitation regime, in the range $n_e = 0$–0.045 e/atom, corresponding to 0–0.75% photoexcited electrons from the valence band, obtaining a phonon frequency shift of -0.79 THz per 1% excitation of the valence population. In the same assumptions as before, we obtain that the derivative of the reflectivity peak frequency with respect to pump fluence is -0.0693 THz per mJ/cm^2, in excellent agreement with the experimental value of 0.07 THz per mJ/cm^2 (an overestimation of 1%). This result implies that cell relaxation effects must be included in order to obtain a quantitative agreement with the experimental observations.

B. Silicon

We switch to the study of the vibrational response of silicon under photoexcitation in the cDFPT approach. According to the discussion made for tellurium, calculations are performed on the volume-relaxed cell at the investigated PC value. We start by discussing the behavior of the phonon frequencies as a function of the PC, shown in Figs. 4(a) and 4(b). The behavior of the topmost phonon frequency at the Γ point as a function of PC is reported in Fig. 4(a). We observe an ≈16.1% softening of optical phonon frequencies already at $n_e = 0.05$ e/atom, demonstrating that at values of PC large enough to screen excitonic effects but substantially lower than the largest PCs that are achieved in experiments, the vibrational response of the system is substantially affected and the phonon spectrum cannot be considered as frozen (i.e., unchanged with respect to the unexcited case). In Fig. 4(b), we report the full phonon spectrum for silicon along high-symmetry directions. We point out that no acoustic sum rule was enforced in the calculation of phonon eigenvalues. Softenings can be observed near the Γ point with increasing PC, signaling the progressive formation of a structural instability. We recall that close to the structural instability, anharmonic effects could become relevant.

We conclude by pointing out that while conventional melting occurs heterogeneously at high atomic mobility (thermodynamic melting), experimental evidence shows that a homogeneous mechanical melting under irradiation can be observed and that a competition between thermodynamic and mechanical melting exists [61,62]. The development of imaginary phonon frequencies is related to a second-order phase

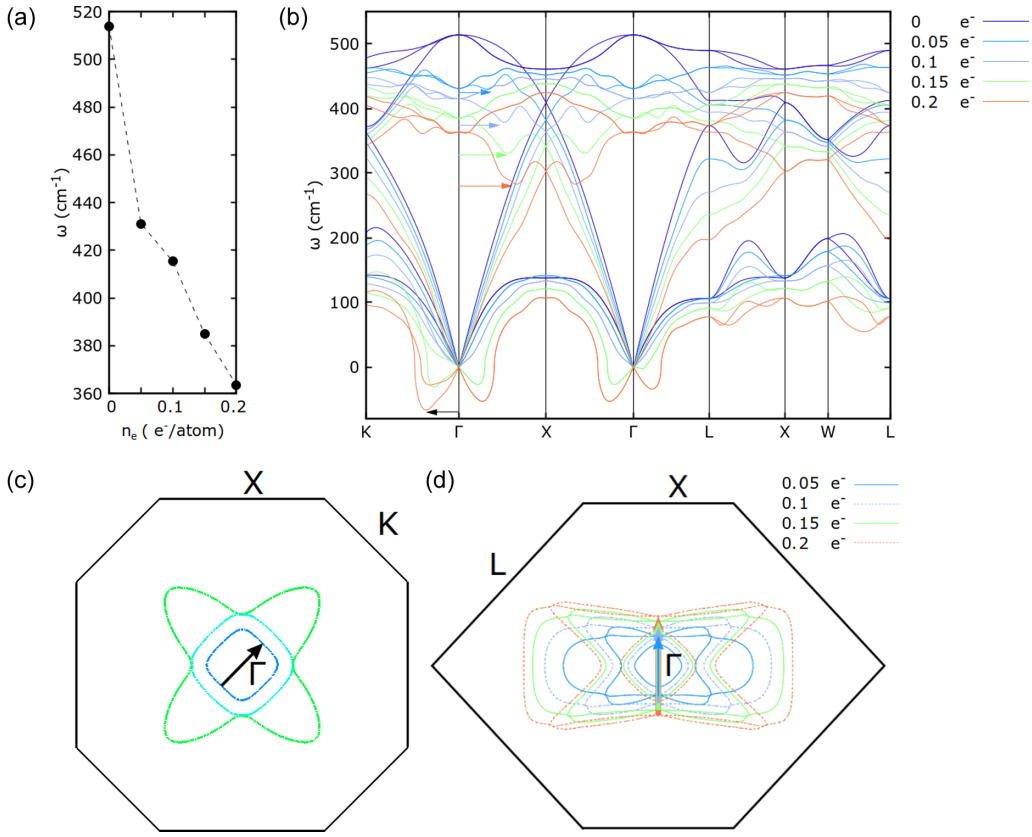

FIG. 4. (a) Optical phonon frequency for silicon at Γ as a function of PC. (b) Phonon frequencies for silicon at selected PC values. (c) Section of the valence quasi-FS at $n_e = 0.2$ e/atom, in the plane perpendicular to the [110] reciprocal direction. The black arrow indicates the nesting vector responsible for the phonon instability. (d) Section of the valence quasi-FS at various PC values, in the plane perpendicular to the [211] reciprocal direction. Arrows indicate nesting vectors responsible for the softenings observed in the optical branch along the Γ-X direction. FS plots have been realized using the open-source software FERMISURFER [60].

transition and thus to the onset of either a reduced spatial periodicity or mechanical melting; however, it is in general possible that a *latent* first-order transition occurs before the phonon softening.

At any finite PC values, we observe the formation of multiple softenings in the phonon branches, which we address here in more detail. The full band-resolved valence and conduction quasi-FSs at a PC value of 0.2 e/atom are reported in Fig. 5. We show that the valence quasi-FS is mainly responsible for phonon softenings. This is clearly illustrated in Fig. 4(c), where we show a cut of the valence quasi-FS perpendicular to the [110] reciprocal direction. We relate the vector nesting the smaller section of the valence quasi-FS along the Γ-K direction to the main phonon softening observed in the phonon spectrum at $n_e = 0.2$ e/atom [see Figs. 4(b) and 4(c), black arrow]. We further relate optical branch softenings to a specific nesting vector for the valence quasi-FS sheets depicted in Figs. 5(b) and 5(c). We perform cuts of the valence quasi-FS perpendicular to the [211] reciprocal direction as a function of PC, finding that the optical branch softening in the Γ-X direction happens at the wave vector where the two external sheets of the valence quasi-FS touch [see Figs. 4(b) and 4(d), colored arrows].

Previous theoretical studies [31,32] reported that silicon under intense photoexcitation is subject to lattice instabilities and structural changes, in agreement with the experimentally observed melting of silicon [63]. However, the transition mechanism is not completely clear. In the *ab initio* molecular dynamical study by Silvestrelli *et al.* [32] it was shown that a high electronic temperature of 2.15 eV causes the melting of the crystal. It was claimed that no soft phonon frequencies were observed. In the DFPT study by Recoules *et al.*

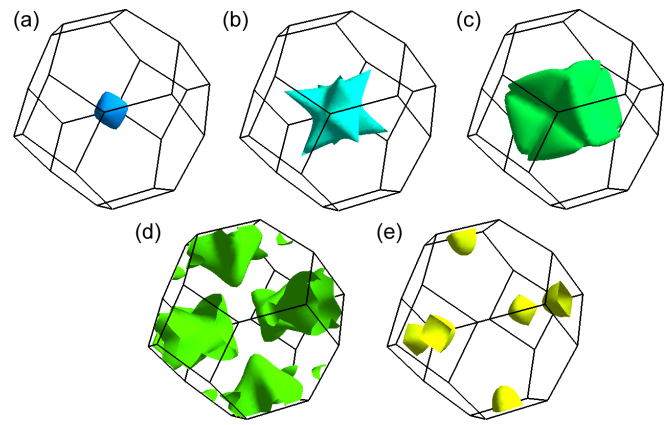

FIG. 5. (a)–(c) The three sheets of the valence quasi-FS for silicon at a PC value of 0.2 e/atom (d) and (e) The two sheets of the conduction quasi-FS at a PC value of 0.2 e/atom FS plots have been realized using the open-source software FERMISURFER [60].

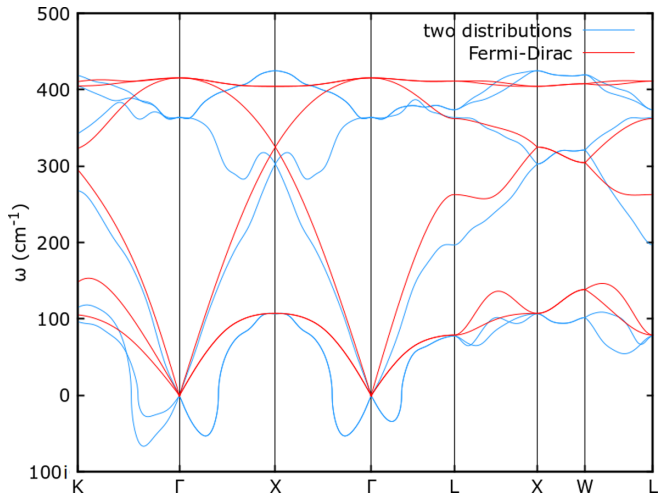

FIG. 6. Phonon frequencies for silicon at 0.2 e/atom obtained with the two-carrier-distribution approach and with the single Fermi-Dirac distribution. In the case of the two-carrier-distribution approach, we observe the appearance of softenings, while no softenings can be seen in the case of a single-Fermi-Dirac-distribution approach.

[31], considering the same electronic temperature of 2.15 eV, soft phonon modes were observed along most of the high-symmetry direction of the zinc-blende crystal, in contradiction with Ref. [32]. In both studies, the volume was kept fixed to its equilibrium value. However, there is no real reason for this assumption as, after the pumping and after the consequent thermalization of the electronic system, when the lattice degrees of freedom set in, the cell deformation does occur [58].

In order to better clarify this issue, in Fig. 6 we compare the calculated phonon spectrum for silicon at 0.2 e/atom in cDFPT (blue lines) with the one obtained within a high-temperature Fermi-Dirac approach (red lines), employing an electronic temperature of 1 eV, corresponding to $n_e = 0.2$ e/atom In both cases, the lattice parameter is determined with a variable-cell relaxation procedure. As expected, the single-Fermi-Dirac-distribution approach leads to smooth phonon dispersion curves with all the quasi-FS softenings washed out by the large Fermi temperature. Furthermore, no unstable phonons occur. In contrast, in the two-Fermi-distribution approach, as the holes' and electrons' temperatures are low, the phonon dispersion still displays quasi-FS-related softenings and the occurrence of a structural instability. Moreover, the softening of the optical mode at the zone center is substantially larger in the case of Si. Conversely, we observe an $\approx$1% volume reduction in the cDFPT approach at 0.2 e/atom, qualitatively explaining the observations of Refs. [58,64], while a 3% volume increase is predicted by the high-temperature Fermi-Dirac approach. For $n_e \leqslant 0.1$ e/atom we observe a linear dependence between PC and lattice compression, compatibly with the linear compression as a function of the fluence reported experimentally [64]. The differences in volume expansion with the two approaches are even more severe at higher fluences. Indeed, at the fluences of 2.15 eV considered in Refs. [31,32] the use of an electronic temperature of 2.15 eV leads to a lattice expansion exceeding 10% of the original lattice parameter (5.98 Å against the low-temperature LDA value of 5.38 Å). In contrast, the two-distribution model leads to a 2% lattice expansion (5.48 Å).

On a general basis, we can thus conclude that the use of a single Fermi-Dirac distribution with temperatures of the order of the incoming laser frequency leads to unrealistic values of the volume expansion. In this framework, the approximation of considering the cell fixed in Si, besides being unjustified (at least before the thermal melting occurs), artificially enhances the tendency towards phonon instabilities with respect to the case in which, in the same framework, the structural optimization is carried out.

Finally, the complete structural optimization using two distributions, each one with cold carriers, leads to stronger phonon softenings and preserves the Kohn anomalies due to FS nesting of conduction of valence quasi-FSs. Moreover, it generally gives a better agreement with experiments with respect to the case of a single Fermi-Dirac distribution with hot electrons.

C. Gallium arsenide

We now consider the vibrational response of GaAs under photoexcitations in cDFPT. Experimental observations demonstrate that crystalline GaAs under irradiation undergoes an insulator-metal transition for high fluence values, while also showing a structural amorphization of nonthermal origin [65]. We calculate the phonon spectrum at varying PC, exploring the range 0–0.2 e/atom, corresponding to 0–10% valence electron excitation. The results are depicted in Fig. 7. In Fig. 7(a) the behavior of Γ acoustic phonon frequency is reported [no longitudinal-optical–transverse-optical (LO-TO) splitting is included here], demonstrating a sizable effect also at low PC. As was observed for Si, even at the lowest PC of $n_e = 0.05$ e/atom, the phonon spectrum is substantially affected and cannot be considered unchanged with respect to the undoped case.

In the phonon dispersion reported in Fig. 7(b), we also include LO-TO splitting at Γ in the absence of photocarriers, while we do not include it at finite PC values, assuming that the screening effect of photoexcited carriers will suppress it at any finite PC value. Similarly to what observed for silicon, phonon softenings emerge close to the Γ point of the BZ for increasing PC values, pointing towards the formation of lattice instabilities. Other softenings are observed in the W-L reciprocal direction and the L-X reciprocal direction. As in silicon, anharmonic effects may change the critical fluence for the formation of a phonon instability. Interestingly, we observe that the volume increases as the PC is increased in the range 0–0.2 e/atom, at variance with what we observe in silicon. We point out that no acoustic sum rule was enforced in the calculation of phonon eigenvalues.

Differently from what we have done for silicon, here we disentangle the role of the two quasi-FSs by comparing the calculated cDFPT phonon spectrum with the ones obtained by a negative (positive) doping of 0.2 e/atom (-0.2 e/atom) performed on the same crystal structure. The results are shown in Fig. 8. We observe that similar softenings around the Γ point, although less pronounced, appear for a positive doping of -0.2 e/atom; thus we conclude that the observed soften-

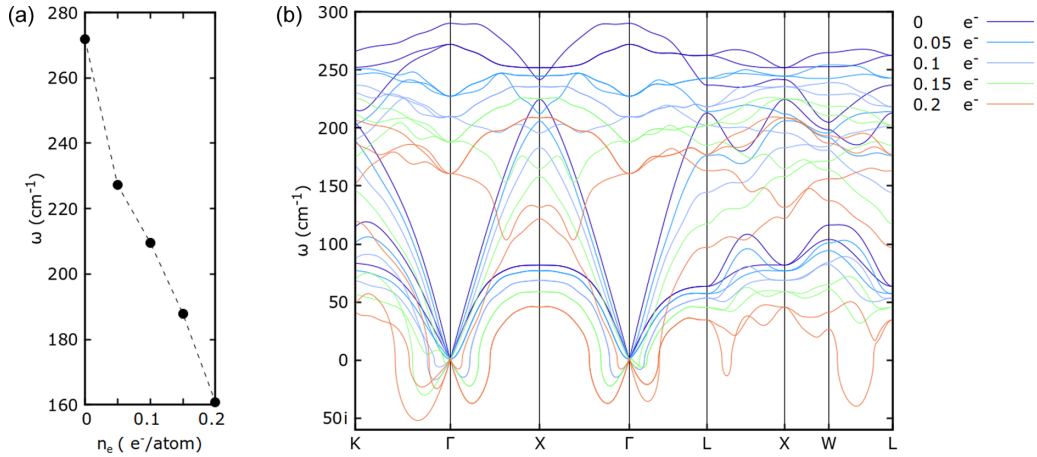

FIG. 7. (a) Optical phonon frequency for GaAs at Γ as a function of PC. Phonon softenings form near Γ for PC values up to 0.15 e/atom, while new softenings along the L-X and W-L high-symmetry directions emerge at 0.2 e/atom

ings are caused by the valence quasi-FS also in GaAs. The close correspondence to the results shown for silicon is not surprising as the electronic structure of GaAs (not shown) closely resembles that of silicon; in particular, its valence quasi-FS contains the same quasi-FS shown in Fig. 5(a), which is responsible for the phonon instability.

D. Vanadium diselenide

Finally, we demonstrate the reliability of electron-phonon coupling matrix element calculations by considering the case of the bulk VSe_2 in its stable polytype (1T). VSe_2 has metallic character; nevertheless, the cDFPT formalism can still be applied, provided that the photocarrier population in conduction is separated from the lower states by an energy gap and thus carrier-carrier recombination is necessary to deexcite conduction electrons: This aspect is highlighted in the band structure reported in Fig. 9(a). We choose VSe_2 since it possesses a free internal coordinate in the out-of-plane selenium position, and

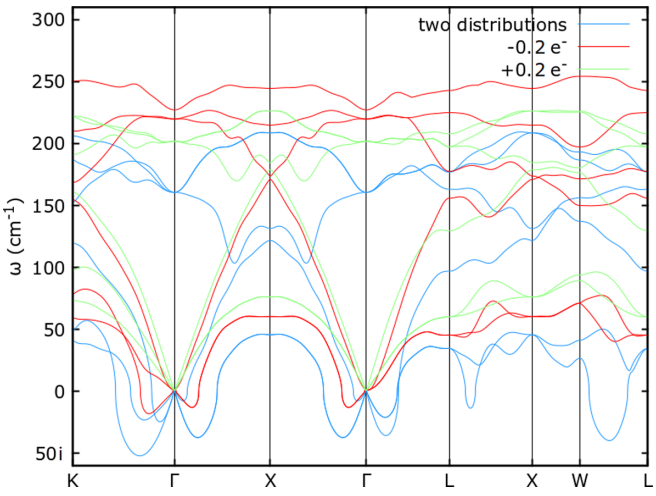

FIG. 8. Phonon frequencies for GaAs with the two-carrier distribution at 0.2 e/atom (blue lines), compared with phonon frequencies obtained with a doping of +0.2 e/atom (green lines) and −0.2 e/atom (red lines).

thus a nonzero Fermi shift (or better, two nonzero Fermi shifts in the case of photoexcitations). Furthermore, this material has sizable electron-phonon matrix elements. We exploit the following relation existing between the deformation potential $d^{n,m}_{\mathbf{k},\mathbf{q}}$ and Kohn-Sham eigenvalues:

$$d^{n,n}_{\mathbf{k},\mathbf{q}=\mathbf{0},\nu} = \frac{d\epsilon_{\mathbf{k},n}}{d\mathbf{u}_{\mathbf{q}=\mathbf{0},\nu}}, \tag{33}$$

where n is the band index, while $d\mathbf{u}_{\mathbf{q}=\mathbf{0},\nu}$ represents the infinitesimal motion of atoms along a generic pattern in the primitive cell. We calculate the deformation potential elements in cDFPT and the eigenvalue derivative in the finite-difference approach. Our results are reported in Figs. 9(b) and 9(c), for 0.083 e/atom excitation, without and with the Fermi shift correction, respectively. The error committed without including the Fermi shift is especially evident for the conduction electron-phonon matrix elements. We verified that the error committed in Fig. 9(b) corresponds exactly to the shift of the valence or conduction quasi-Fermi-levels induced by the perturbation. The excellent agreement between the finite-difference method and the cDFPT calculation demonstrated in Fig. 9(c) confirms the consistency of our formulation.

VIII. CONCLUSIONS

In this paper, building on top of Refs. [28,29], we develop a complete constrained density-functional perturbation theory scheme for structural optimization, calculation of the harmonic vibrational properties, and electron-phonon interaction in insulators in the presence of an excited and thermalized electron-hole plasma such as that typically obtained after ultrafast optical pumping. The method assumes that the photocarriers thermalize faster than the lattice, the electron-hole recombination rate is longer than the phonon period, and the photocarrier concentration is large enough to screen excitons. We demonstrate its applicability by calculating the evolution of the vibrational spectra as a function of fluence of Te, Si, and GaAs. In the case of Te, considering displacive excitations of coherent phonons, we show that allowing for cell relaxation dramatically improves the agreement with experiments for the derivative of the reflectivity peak frequency with respect to

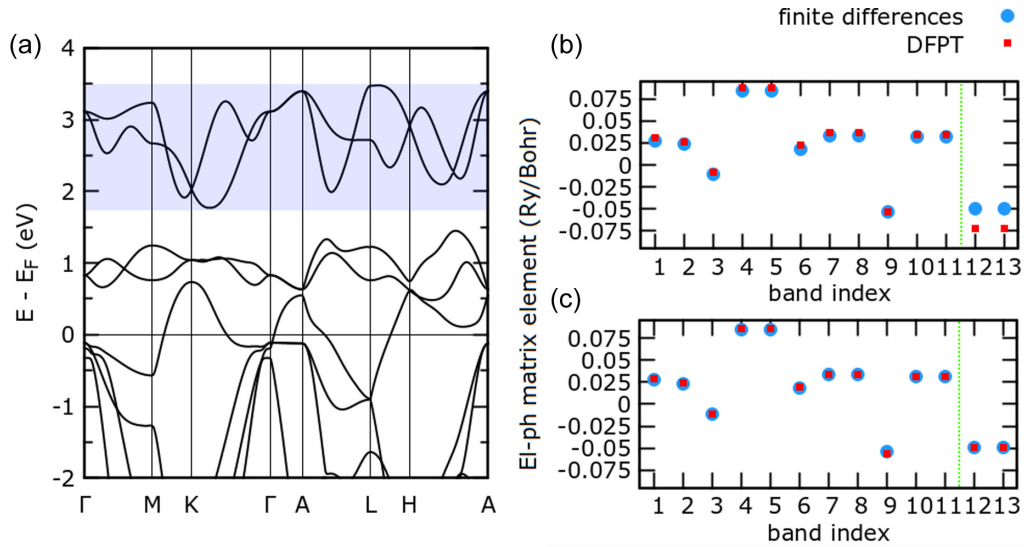

FIG. 9. (a) Band structure for bulk VSe_2. The semitransparent blue rectangle highlights the conduction states considered in the cDFT and cDFPT simulations. (b) and (c) Diagonal deformation potential matrix elements $d^{n,n}_{\mathbf{k},\mathbf{q}=\mathbf{0}}$ along the out-of-plane coordinate of one selenium atom, with 0.083 e/atom moved to the conduction states, without (b) and with (c) Fermi shift. The green dashed lines separate valence and conduction regions of the cDFT and cDFPT simulation. El-ph, electron-phonon.

fluence (from 14% disagreement in the absence of structural relaxation to 1% with geometrical optimization). In the case of Si and GaAs, we show that even at a fluence corresponding to a PC of $n_e = 0.05$ e/atom, which is substantially lower than the largest ones achievable in experiments, the phonon spectrum is severely affected with large softenings of optical zone-center phonons and the emergence of large Kohn anomalies. In order to correctly describe these anomalies in Si and GaAs, phonon momenta grids as large as $12 \times 12 \times 12$ are needed. In a finite-difference approach this would mean calculating on supercells composed of 3456 atoms, highlighting the power of our cDFPT approach (and of DFPT approaches in general).

At larger fluences, the Si and GaAs lattices are destabilized, and imaginary harmonic phonon frequencies emerge, probably a signature of nonthermal melting. However, care is needed as in this regime anharmonic effects could become relevant. As our cDFPT scheme allows fast access to forces and structural optimization, in the future it could be coupled to the stochastic self-consistent harmonic approximation [66] in order to tackle light-induced anharmonicity.

Finally, as our cDFPT method allows for the study of slowly convergent electronic and vibrational instabilities in photoexcited materials at an affordable computational cost, similarly to what is done by DFPT in ground-state studies, it could then be used to screen for hidden broken-symmetry states and irreversible phase transitions (including nonthermal melting) in materials.

ACKNOWLEDGMENTS

We acknowledge support from the European Union's Horizon 2020 research and innovation program Graphene Flagship under Grant Agreement No. 881603. We acknowledge the CINECA award under the ISCRA initiative, for the availability of high-performance computing resources and support. We thank Luca Perfetti and Jelena Sjakste for useful discussions.

[1] P. Giannozzi, S. de Gironcoli, P. Pavone, and S. Baroni, Phys. Rev. B **43**, 7231 (1991).
[2] S. Baroni, P. Giannozzi, and A. Testa, Phys. Rev. Lett. **58**, 1861 (1987).
[3] S. de Gironcoli, Phys. Rev. B **51**, 6773(R) (1995).
[4] S. Baroni, S. de Gironcoli, A. Dal Corso, and P. Giannozzi, Rev. Mod. Phys. **73**, 515 (2001).
[5] S. Y. Savrasov and D. Y. Savrasov, Phys. Rev. B **54**, 16487 (1996).
[6] X. Gonze and C. Lee, Phys. Rev. B **55**, 10355 (1997).
[7] F. Mauri, O. Zakharov, S. de Gironcoli, S. G. Louie, and M. L. Cohen, Phys. Rev. Lett. **77**, 1151 (1996).
[8] Y. Nomura and R. Arita, Phys. Rev. B **92**, 245108 (2015).
[9] I. Timrov, N. Marzari, and M. Cococcioni, Phys. Rev. B **98**, 085127 (2018).
[10] M. Calandra, G. Profeta, and F. Mauri, Phys. Rev. B **82**, 165111 (2010).
[11] M. Maiuri, M. Garavelli, and G. Cerullo, J. Am. Chem. Soc. **142**, 3 (2020).
[12] K. Sokolowski-Tinten and D. von der Linde, Phys. Rev. B **61**, 2643 (2000).
[13] E. Matsubara, S. Okada, T. Ichitsubo, T. Kawaguchi, A. Hirata, P. F. Guan, K. Tokuda, K. Tanimura, T. Matsunaga, M. W. Chen, and N. Yamada, Phys. Rev. Lett. **117**, 135501 (2016).
[14] C. Ferrante, A. Virga, L. Benfatto, M. Martinati, D. De Fazio, U. Sassi, C. Fasolato, A. K. Ott, P. Postorino, D. Yoon, G. Cerullo, F. Mauri, A. C. Ferrari, and T. Scopigno, Nat. Commun. **9**, 308 (2018).
[15] L. Huang, J. P. Callan, E. N. Glezer, and E. Mazur, Phys. Rev. Lett. **80**, 185 (1998).

[16] C. W. Siders, A. Cavalleri, K. Sokolowski-Tinten, Cs. Tóth, T. Guo, M. Kammler, M. Horn von Hoegen, K. R. Wilson, D. von der Linde, and C. P. J. Barty, Science **286**, 1340 (1999).

[17] A. Rousse, C. Rischel, S. Fourmaux, I. Uschmann, S. Sebban, G. Grillon, P. Balcou, E. Förster, J. P. Geindre, P. Audebert, J. C. Gauthier, and D. Hulin, Nature (London) **410**, 65 (2001).

[18] C. Mariette, M. Lorenc, H. Cailleau, E. Collet, L. Guérin, A. Volte, E. Trzop, R. Bertoni, X. Dong, B. Lépine, O. Hernandez, E. Janod, L. Cario, V. T. Phuoc, S. Ohkoshi, H. Tokoro, L. Patthey, A. Babic, I. Usov, D. Ozerov *et al.*, Nat. Commun. **12**, 1239 (2021).

[19] T. Huber, S. O. Mariager, A. Ferrer, H. Schäfer, J. A. Johnson, S. Grübel, A. Lübcke, L. Huber, T. Kubacka, C. Dornes, C. Laulhe, S. Ravy, G. Ingold, P. Beaud, J. Demsar, and S. L. Johnson, Phys. Rev. Lett. **113**, 026401 (2014).

[20] E. Möhr-Vorobeva, S. L. Johnson, P. Beaud, U. Staub, R. De Souza, C. Milne, G. Ingold, J. Demsar, H. Schaefer, and A. Titov, Phys. Rev. Lett. **107**, 036403 (2011).

[21] S. Wall, S. Yang, L. Vidas, M. Chollet, J. M. Glownia, M. Kozina, T. Katayama, T. Henighan, M. Jiang, T. A. Miller, D. A. Reis, L. A. Boatner, O. Delaire, and M. Trigo, Science **362**, 572 (2018).

[22] D. M. Fritz, D. A. Reis, B. Adams, R. A. Akre, J. Arthur, C. Blome, P. H. Bucksbaum, A. L. Cavalieri, S. Engemann, S. Fahy, R. W. Falcone, P. H. Fuoss, K. J. Gaffney, M. J. George, J. Hajdu, M. P. Hertlein, P. B. Hillyard, M. Horn-von Hoegen, M. Kammler, J. Kaspar *et al.*, Science **315**, 633 (2007).

[23] M. Cammarata, S. Zerdane, L. Balducci, G. Azzolina, S. Mazerat, C. Exertier, M. Trabuco, M. Levantino, R. Alonso-Mori, J. M. Glownia, S. Song, L. Catala, T. Mallah, S. F. Matar, and E. Collet, Nat. Chem. **13**, 10 (2021).

[24] B. I. Cho, K. Engelhorn, A. A. Correa, T. Ogitsu, C. P. Weber, H. J. Lee, J. Feng, P. A. Ni, Y. Ping, A. J. Nelson, D. Prendergast, R. W. Lee, R. W. Falcone, and P. A. Heimann, Phys. Rev. Lett. **106**, 167601 (2011).

[25] I. Katayama, H. Aoki, J. Takeda, H. Shimosato, M. Ashida, R. Kinjo, I. Kawayama, M. Tonouchi, M. Nagai, and K. Tanaka, Phys. Rev. Lett. **108**, 097401 (2012).

[26] R. Mankowsky, A. Subedi, M. Först, S. O. Mariager, M. Chollet, H. T. Lemke, J. S. Robinson, J. M. Glownia, M. P. Minitti, A. Frano, M. Fechner, N. A. Spaldin, T. Loew, B. Keimer, A. Georges, and A. Cavalleri, Nature (London) **516**, 71 (2014).

[27] M. Först, C. Manzoni, S. Kaiser, Y. Tomioka, Y. Tokura, R. Merlin, and A. Cavalleri, Nat. Phys. **7**, 854 (2011).

[28] P. Tangney and S. Fahy, Phys. Rev. B **65**, 054302 (2002).

[29] P. Tangney and S. Fahy, Phys. Rev. Lett. **82**, 4340 (1999).

[30] E. D. Murray, S. Fahy, D. Prendergast, T. Ogitsu, D. M. Fritz, and D. A. Reis, Phys. Rev. B **75**, 184301 (2007).

[31] V. Recoules, J. Clérouin, G. Zérah, P. M. Anglade, and S. Mazevet, Phys. Rev. Lett. **96**, 055503 (2006).

[32] P. L. Silvestrelli, A. Alavi, M. Parrinello, and D. Frenkel, Phys. Rev. Lett. **77**, 3149 (1996).

[33] U. Strauss, W. W. Rühle, and K. Köhler, Appl. Phys. Lett. **62**, 55 (1993).

[34] R. Häcker and A. Hangleiter, J. Appl. Phys. (Melville, NY) **75**, 7570 (1994).

[35] J. Hader, J. V. Moloney, and S. W. Koch, Appl. Phys. Lett. **87**, 201112 (2005).

[36] G. Bourdon, I. Robert, I. Sagnes, and I. Abram, J. Appl. Phys. (Melville, NY) **92**, 6595 (2002).

[37] A. Richter, S. W. Glunz, F. Werner, J. Schmidt, and A. Cuevas, Phys. Rev. B **86**, 165202 (2012).

[38] S. Hunsche, K. Wienecke, T. Dekorsy, and H. Kurz, Phys. Rev. Lett. **75**, 1815 (1995).

[39] S. M. O'Mahony, F. Murphy-Armando, E. D. Murray, J. D. Querales-Flores, I. Savić, and S. Fahy, Phys. Rev. Lett. **123**, 087401 (2019).

[40] A. Splendiani, L. Sun, Y. Zhang, T. Li, J. Kim, C.-Y. Chim, G. Galli, and F. Wang, Nano Lett. **10**, 1271 (2010).

[41] L. Yuan and L. Huang, Nanoscale **7**, 7402 (2015).

[42] A. Chernikov, C. Ruppert, H. M. Hill, A. F. Rigosi, and T. F. Heinz, Nat. Photonics **9**, 466 (2015).

[43] H. Haug and S. W. Koch, *Quantum Theory of the Optical and Electronic Properties of Semiconductors*, 5th ed. (World Scientific, Singapore, 2009).

[44] M. Fox, Am. J. Phys. **70**, 1269 (2002).

[45] V. B. Anzin, M. I. Eremets, Y. V. Kosichkin, A. I. Nadezhdinskii, and A. M. Shirokov, Phys. Status Solidi A **42**, 385 (1977).

[46] M. Thomas, Chem. Vap. Deposition **3**, 288 (1997).

[47] O. H. Nielsen and R. M. Martin, Phys. Rev. B **32**, 3780 (1985).

[48] O. H. Nielsen and R. M. Martin, Phys. Rev. B **32**, 3792 (1985).

[49] P. Scherpelz, M. Govoni, I. Hamada, and G. Galli, J. Chem. Theory Comput. **12**, 3523 (2016).

[50] C. Hartwigsen, S. Goedecker, and J. Hutter, Phys. Rev. B **58**, 3641 (1998).

[51] P. Giannozzi, S. Baroni, N. Bonini, M. Calandra, R. Car, C. Cavazzoni, D. Ceresoli, G. L. Chiarotti, M. Cococcioni, I. Dabo, A. D. Corso, S. de Gironcoli, S. Fabris, G. Fratesi, R. Gebauer, U. Gerstmann, C. Gougoussis, A. Kokalj, M. Lazzeri, L. Martin-Samos *et al.*, J. Phys.: Condens. Matter **21**, 395502 (2009).

[52] P. Giannozzi, O. Baseggio, P. Bonfà, D. Brunato, R. Car, I. Carnimeo, C. Cavazzoni, S. de Gironcoli, P. Delugas, F. Ferrari Ruffino, A. Ferretti, N. Marzari, I. Timrov, A. Urru, and S. Baroni, J. Chem. Phys. **152**, 154105 (2020).

[53] N. Marzari, D. Vanderbilt, A. De Vita, and M. C. Payne, Phys. Rev. Lett. **82**, 3296 (1999).

[54] J. P. Perdew, K. Burke, and M. Ernzerhof, Phys. Rev. Lett. **77**, 3865 (1996).

[55] J. P. Perdew and A. Zunger, Phys. Rev. B **23**, 5048 (1981).

[56] H. J. Monkhorst and J. D. Pack, Phys. Rev. B **13**, 5188 (1976).

[57] The code can be obtained upon reasonable request from the authors.

[58] W. Jo, Y. C. Cho, S. Kim, E. C. Landahl, and S. Lee, Crystals **11**, 186 (2021).

[59] D. Alfè, Comput. Phys. Commun. **180**, 2622 (2009).

[60] M. Kawamura, Comput. Phys. Commun. **239**, 197 (2019).

[61] S. R. Phillpot, S. Yip, and D. Wolf, Comput. Phys. **3**, 20 (1989).

[62] D. Wolf, P. R. Okamoto, S. Yip, J. F. Lutsko, and M. Kluge, J. Mater. Res. **5**, 286 (1990).

[63] C. V. Shank, R. Yen, and C. Hirlimann, Phys. Rev. Lett. **51**, 900 (1983).

[64] B. Kundys, Appl. Phys. Rev. **2**, 011301 (2015).

[65] A. M.-T. Kim, J. P. Callan, C. A. D. Roeser, and E. Mazur, Phys. Rev. B **66**, 245203 (2002).

[66] L. Monacelli, R. Bianco, M. Cherubini, M. Calandra, I. Errea, and F. Mauri, J. Phys.: Condens. Matter **33**, 363001 (2021).